

Influence of Ti^{4+} ion substitution on structural, electrical and dielectric properties of $\text{Li}_{0.5}\text{Fe}_{2.5}\text{O}_4$ nanoparticles

Jitendra S. Kounsalye¹ · Prashant B. Kharat¹ · Mahendra V. Shisode¹ · K. M. Jadhav¹

Received: 1 July 2017 / Accepted: 3 August 2017 / Published online: 9 August 2017
© Springer Science+Business Media, LLC 2017

Abstract The extent study deals with the structural, electrical and dielectric properties of tetravalent Ti^{4+} ion substituted lithium ferrite nanoparticles synthesized via sol–gel auto combustion technique with chemical formula $\text{Li}_{0.5+0.5x}\text{Ti}_x\text{Fe}_{2.5-1.5x}\text{O}_4$ (where $0.0 \leq x \leq 1.0$ in step of 0.2). The synthesized nanoparticles were characterized by X-ray diffraction technique (XRD). The XRD analysis reveals single phase cubic spinel structure of synthesized samples. The crystallite size calculated from Scherrer's formula and grain size by linear intercept method using field emission scanning electron microscopy (FE-SEM) images, confirms the nanocrystalline nature of the samples. Infrared (IR) spectroscopy shows principle absorption bands for spinel structure. The DC resistivity at room temperature and as a function of temperature was studied using the two-probe technique. DC electrical resistivity of the samples increases with titanium substitution. The frequency dependence of dielectric properties was studied using LCR-Q meter, the dielectric parameters were found to decrease after substitution of titanium ions.

1 Introduction

Ferrites with spinel structure have great importance since they possess both electric and magnetic properties, hence, they can be used in electronic and magnetic applications [1]. Among the spinel ferrites family, lithium ferrite (Li-ferrites) is one of the most important spinel ferrite with high

saturation magnetization (67.8 emu/g) [2] and high Curie temperature ($T_c \sim 620$ °C) [3]. The Li-ferrite with inverse spinel structure have great importance in today's technology and has potential applications in lithium ion batteries, magnetic cores, microwave frequency applications, power transformation in electronics, antenna and memory devices etc. [4–6]. They possess inverse spinel structure with Li^+ and some Fe^{3+} occupying octahedral sites [B] and rest Fe^{3+} ions occupy tetrahedral (A) sites [7]. In literature, two crystallographic arrangements of Li-ferrite have been reported, a super structured form in which the Li^+ and Fe^{3+} ions are ordered [8] and a disordered form in which Li^+ and Fe^{3+} ions have a random distribution over all the octahedral sites [9].

The properties of nanocrystalline spinel ferrites are dependent on various aspects such as the method of preparation [10, 11], synthesis parameters [12, 13], substituted cations [14–16], annealing temperature, and duration [17, 18] etc. Recently sol–gel auto combustion [19], micro-emulsion [20], hydrothermal [21], co-precipitation synthesis methods [22] have been employed for the preparation of nanocrystalline spinel ferrites. Among these methods, sol–gel auto combustion method offers great advantages such as homogeneity, fine crystallite size, easy to tailor synthesis parameters, requires low temperature and is cost-effective [23, 24]. Li-ferrite, as well as substituted Li-ferrite, has interesting technological applications in various fields. The introduction of Ti^{4+} ions in the Li-ferrite reduces the formation of Fe^{2+} ions [25]. Thus, it is expected that it may improve dielectric and magnetic properties of Li-ferrite. Structural and electric properties of $\text{Li}_{0.35}\text{Cd}_x\text{Ti}_x\text{Mn}_{0.1}\text{Fe}_{2.55-2x}\text{O}_4$ system [26], magnetic and electrical properties of $\text{Li}_{0.5}\text{Zn}_x\text{Ti}_x\text{Mn}_{0.05}\text{Fe}_{2.45-2x}\text{O}_4$ system [27] also, Ti^{4+} substituted Li-ferrite [28–30] have been reported in the literature. However, to the best of our knowledge and updated literature survey, there are no reports available on the systematic

✉ K. M. Jadhav
drjadhavkm@gmail.com

¹ Department of Physics, Dr. Babasaheb Ambedkar Marathwada University, Aurangabad, M.S., India

investigations of structural and electrical properties of Ti^{4+} substituted Li-ferrite nanoparticles with chemical formula $Li_{0.5+0.5x}Ti_xFe_{2.5-1.5x}O_4$.

With this motivation, herein we report the structural and electrical properties of Ti^{4+} substituted Li-ferrite nanoparticles synthesized via simple and cost-effective sol–gel auto combustion method for first time. Further, the structural, morphological, DC electrical and dielectric properties were investigated and discussed in detail.

2 Experimental

2.1 Materials

Lithium nitrate ($LiNO_3$) as source of Li^+ ions, ferric nitrate nonahydrate [$Fe(NO_3)_3 \cdot 9H_2O$] as source of Fe^{3+} ions, tetra butyl titanate ($C_{16}H_{36}O_4Ti$) as source of Ti^{4+} ions and citric acid ($C_6H_8O_7$) as a fuel, distilled water (DH_2O) and ethanol (C_2H_6O) as a solvent. All the chemicals of AR grade with ~99.99% purity were purchased from Sigma-Aldrich (Merck) and used for synthesis without further purification.

2.2 Synthesis of $Li_{0.5+0.5x}Ti_xFe_{2.5-1.5x}O_4$ nanoparticles

As shown in Fig. 1, nanoparticles of Ti^{4+} substituted Li-ferrite were synthesized using the sol–gel auto combustion method. The metal nitrates to fuel ratio was taken as 1:3 by implementing the propellant chemistry approach. All the oxidants were dissolved separately in 100 ml DH_2O [solution (B, C, D)], ethanol was used as a solvent to dissolve tetra butyl titanate [solution (A)] whereas ammonia solution was used to adjust the pH of the solution (AB) at 8 and for making the sol neutral. The neutral sol [a mixture of (AB) and (CD)] was continuously stirred at 90 °C up to gel formation when the gel befalls the temperature is increased to 180 °C; the combustion proceeds and we get the yield in the form of ash. The ash was ground in mortar pestle to form a fine powder; this powder was annealed at 800 °C for 6 h for removal of nitrate impurities, as well as for crystalline growth. The annealed powder was further used for characterizations.

2.3 Characterizations

The annealed samples were characterized by X-ray diffractometer (XRD) Rigaku (Miniflex-2) using CuK_{α} ($\lambda=0.15418$ nm) radiation in the 2θ range of 20°–80°. The JEOL JSM-6360, Mira-3, Tescan, Brno-Czech Republic, Field emission scanning electron microscope (FE-SEM) was used to study the morphology of typical samples and Multi RAM FT-Raman spectrometer was used to study compositional analysis in the range of 400–800 cm^{-1} . The

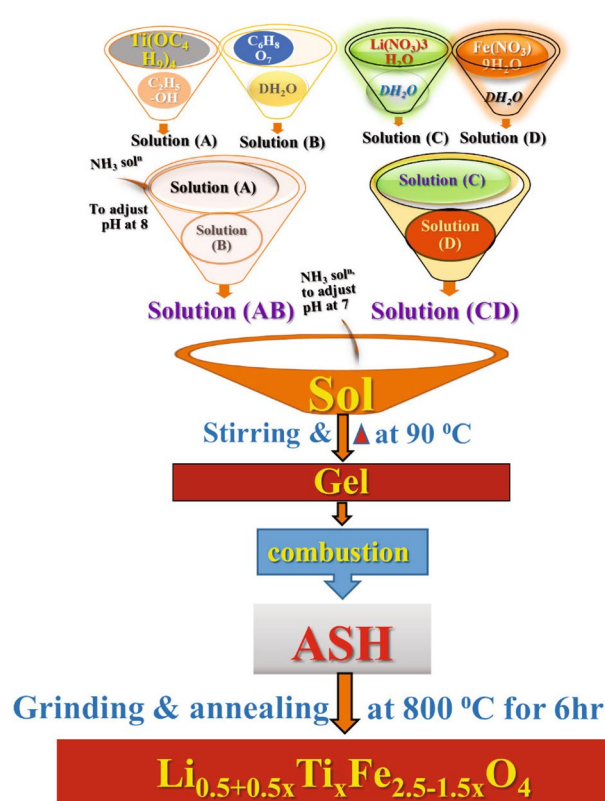


Fig. 1 Schematic flow chart of sol–gel auto combustion route for $Li_{0.5+0.5x}Ti_xFe_{2.5-1.5x}O_4$ nanoparticles

temperature dependent electrical properties (DC resistivity) were studied using two probe setup in the temperature range 700–1000 K with a step size of 10 K. The I–V characteristics were studied using the KEITHELY Source Meter (Model No. 2400), in the voltage range from +5 to –5V and the room temperature resistivity was calculated from the I–V plot. The frequency dependence of dielectric properties was studied using the LCR-Q meter in the frequency range 50 Hz–5 MHz.

3 Results and discussion

3.1 XRD analysis

The XRD patterns of the $Li_{0.5+0.5x}Ti_xFe_{2.5-1.5x}O_4$ nanoparticles are shown in Fig. 2. The XRD pattern of pure Li-ferrite sample matches well with JCPDS card #82-1436 belonging to the octahedral [B]-site-ordered (α) phase while the remaining patterns match with JCPDS card #74-1911 corresponding to the [B]-site-disordered (β) structural phase. The α -phase is an ordered phase in which Li^+ and Fe^{3+} ions are ordered in 1:3 ratio on the [B] site of the FCC inverse spinel structure with a space group of $P4_332$ [31]. The β -phase is a disordered phase

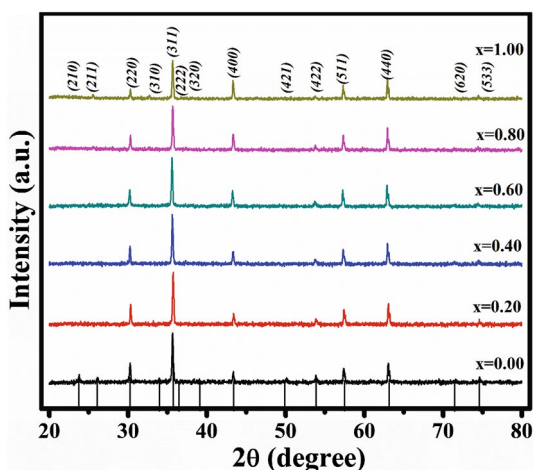


Fig. 2 X-ray diffraction pattern of $\text{Li}_{0.5+0.5x}\text{Ti}_x\text{Fe}_{2.5-1.5x}\text{O}_4$ nanoparticles

where Li^+ and Fe^{3+} ions distributed on the [B] sites of the FCC mixed spinel structure with Fd3m space group [32]. The $\text{P4}_32 \rightarrow \text{Fd3m}$ symmetry transformation of $\text{Li}_{0.5}\text{Fe}_{2.5}\text{O}_4$ spinel ferrite in the present system is observed with the substitution of Ti^{4+} ions, such type of transition is reported in the literature with heat-treatment [33].

The XRD patterns revealed the reflections belonging to cubic spinel structure, no impurity peaks have been observed in the XRD pattern. The intensity of (311) plane is higher than that of other planes (211), (220), (222), (400), (422), (511), (440) and (533) which was chosen for the determination of crystallite size. As the Ti^{4+} concentration increases, the minor reflections along (210), (310), (320), (421) and (620) planes disappeared, confirming the symmetry transformation.

The lattice parameter (a) was calculated using the Eq. (1) [34],

$$a = d\sqrt{(h^2 + k^2 + l^2)} \text{ \AA} \tag{1}$$

where, all symbols carry their usual meanings.

Table 1 Lattice parameter (a), X-ray density (d_x), hopping length (L_A , L_B), tetrahedral bond (d_{AL}), octahedral bond (d_{BL}), tetra edge (d_{AE}) and octa edge (d_{BEU}) shared and unshared, Ionic radii (r_A ,

X	a (Å)	d_x (gm/cm ³)	L_A (Å)	L_B (Å)	d_{AL} (Å)	d_{BL} (Å)	d_{AE} (Å)	d_{BEU}		r_A	r_B	t (nm)
								Shared	Unshared			
0.00	8.337	4.747	3.610	2.948	1.892	2.035	3.089	2.806	2.949	0.572	0.714	44.0
0.20	8.346	4.583	3.614	2.951	1.894	2.038	3.093	2.809	2.953	0.574	0.717	46.0
0.40	8.355	4.421	3.618	2.954	1.896	2.040	3.096	2.812	2.956	0.576	0.719	45.7
0.60	8.365	4.259	3.622	2.957	1.898	2.042	3.099	2.815	2.959	0.578	0.721	45.2
0.80	8.376	4.095	3.627	2.961	1.900	2.045	3.103	2.819	2.963	0.580	0.722	45.9
1.00	8.381	3.942	3.629	2.963	1.901	2.046	3.105	2.821	2.965	0.582	0.725	44.9

The calculated values of the lattice parameter (a) are listed in Table 1. The values are between 8.337 to 8.381 Å, compatible with the standard JCPDS data. The value of lattice parameter increases with increasing Ti^{4+} concentration, since the ionic radii of substituted Ti^{4+} ion is larger (0.076 nm) when compared to that of Fe^{3+} (0.0645 nm).

The X-ray density (d_x) [35] of the samples was calculated by the Eq. (2),

$$d_x = \frac{8M}{N_A a^3} \text{ gm/cm}^3 \tag{2}$$

where, M is a molecular mass of the sample and N_A is the Avogadro’s number. The obtained values are summarized in Table 1. The X-ray density decreases with increasing Ti^{4+} concentration. This is due to the decrease in molecular mass which is proportional to the X-ray density. The crystallite size was calculated by the Debye-Scherrer’s formula using the most intense peak (311) [36], the obtained values of the crystallite size are tabulated in Table 1. The values show nanocrystalline size (44–46 nm) of the present system.

Using the values of the lattice parameter (a) and oxygen positional parameter ‘u’ (0.0381 nm); the structural parameters viz. hopping lengths (L_A , L_B), tetrahedral bond length (d_{AL}), octahedral bond length (d_{BL}), tetra edge (d_{AE}) and octa edge (d_{BEU}) were determined for all the samples using the standard Eqs. (3–9) [37, 38],

$$L_A = a\sqrt{3/4} \text{ \AA} \tag{3}$$

$$L_B = a\sqrt{2/4} \text{ \AA} \tag{4}$$

$$d_{AL} = a\sqrt{3(u - 1/4)} \text{ \AA} \tag{5}$$

$$d_{BL} = a\sqrt{3u^2 - (11/4)u + (43/64)} \text{ \AA} \tag{6}$$

$$d_{AE} = a\sqrt{2(2u - 1/2)} \text{ \AA} \tag{7}$$

$$d_{BE} = a\sqrt{2(1 - 2u)} \text{ \AA} \tag{8}$$

$$d_{BEU} = a\sqrt{4u^2 - 3u + (11/6)} \text{ \AA} \tag{9}$$

r_B) of tetrahedral and octahedral site, average crystallite size (t) of $\text{Li}_{0.5+0.5x}\text{Ti}_x\text{Fe}_{2.5-1.5x}\text{O}_4$ nanoparticles

The behavior of these parameters with concentration ‘*x*’ of Ti⁴⁺ is analogous to the behavior of lattice parameter ‘*a*’ with ‘*x*’ and is found to increase with increase in Ti⁴⁺ concentration. The calculated values of the parameters are given in Table 1.

The tetrahedral A-site ionic radii and octahedral B-site ionic radii [39, 40] were calculated by the Eq. (10) and (11) respectively [41],

$$r_A = \left(u - \frac{1}{4}\right)a\sqrt{3} - r(O^{2-}) \text{ \AA} \tag{10}$$

$$r_B = \left(\frac{5}{8} - u\right)a - r(O^{2-}) \text{ \AA} \tag{11}$$

where *r*(O) represents the radius of oxygen anions. The values of the ionic radius are given in Table 1 and found to increase with an increase in concentration *x*.

3.2 IR absorption spectra analysis

According to Waldron [42], the ferrites can be considered as continuously bonded crystals with the atoms bonded to all nearest neighbors by equivalent forces (ionic, covalent or Van der Waals). In spinel ferrites, the ions occupy two different sublattices namely tetrahedral (A-site) and octahedral (B-site), depending on the geometrical configuration of the oxygen nearest neighbors. The band at around 600 and 400 cm⁻¹ can be attributed to the stretching vibrations of the tetrahedral group and of the octahedral group respectively [42, 43]. IR spectra for the typical samples of present series were recorded in the range of 400–800 cm⁻¹ are shown in Fig. 3. The absorption band positions are listed in Table 2. The spectra indicate the presence of two absorption bands at ~600 and ~480 cm⁻¹ for all the samples, which confirms the formation of spinel ferrite. Similar results are reported in the literature for Li_{0.5+0.5x}Ti_xFe_{2.5-1.5x}O₄ synthesized by ceramic technique [44]. The Debye temperature has been calculated using the equation given by Waldron [42] [Eq. (12)],

$$\theta_D = \frac{\hbar cv_{av}}{k} \tag{12}$$

where *v_{av}* = (*v_A* + *v_B*)/2, *v_A* and *v_B* are the frequencies of the primary band of A-site and B-site, *h*, *c* and *k* have their usual meanings. The calculated values of the Debye temperature are listed in Table 2. It can be noticed that the value of the Debye temperature is high for *x*=0.40 and the values are following the trend of absorption band position.

3.3 FE-SEM analysis

FE-SEM images of typical samples of the present system are presented in Figs. 4, 5, 6. The FE-SEM images show a porous network of agglomerated fine particles formed

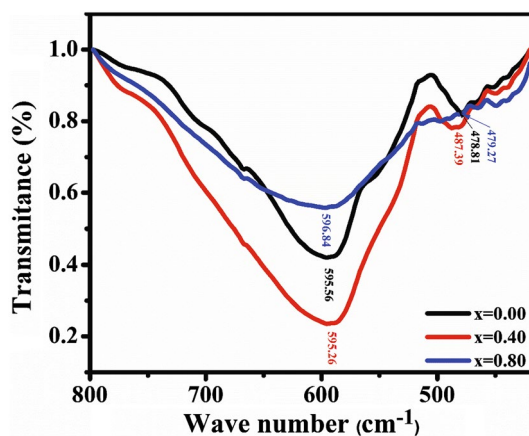


Fig. 3 IR patterns of typical Li_{0.5+0.5x}Ti_xFe_{2.5-1.5x}O₄ (0.00, 0.40 and 0.80) nanoparticles

due to the release of gases during the combustion. The fine particles show spherical morphology. As discussed in the previous section, the crystallite size of the powder particles is estimated in the range of 44–46 nm; the grain size calculated using linear intercept method is also in the range of nanometer size (88–96 nm) which also confirms the nano size of the samples.

3.4 Electrical properties

DC electrical resistivity at room temperature and the temperature dependence (Arrhenius plot) is illustrated in Figs. 7 and 8 respectively. The nanoparticles were pressed into a circular pellet of dimensions ~12 mm × 3 mm. The silver paste was surfaced on both the faces of pellet for good Ohmic contact. The Arrhenius plots show two distinct regions with its own conduction mechanism and different activation energy. The first one belongs to the ferrimagnetic phase known as ordered region and the second one is a disordered region which belongs to the paramagnetic phase [45]. The Arrhenius plot shows a change in slope in each region which corresponds to the Curie point, similar observations have been reported by many researchers for spinel ferrite [46, 47]. The electrical resistivity decreases with increase in temperature, it proposes that the sample obeys Arrhenius relation [48] by indicating semiconducting behavior. The DC electrical resistivity decrease with temperature, since the drift mobility of the charge carriers increases with temperature. The spinel ferrites possess the exponential dependence of DC electrical resistivity with temperature. In spinel ferrites, the charge carrier jumps from ion to ion and not through the crystal lattice, the conduction occurs due to the electronic exchange between Fe³⁺ and Fe²⁺. Thus, the hopping mechanism can be used to explain conduction of spinel ferrite wherein charge carrier jumps from ion to ion. The activation energy in each

Table 2 IR absorption bands (ν_1 and ν_2), Debye temperature (θ_D), grain size (G), activation energy of paramagnetic region (E_p) and ferromagnetic region (E_f), activation energy (ΔE) of $\text{Li}_{0.5+0.5x}\text{Ti}_x\text{Fe}_{2.5-1.5x}\text{O}_4$ nanoparticles

X	ν_1	ν_2	θ_D	G (nm)	E_p (eV)	E_f (eV)	ΔE (eV)
0.00	595.56	478.81	123.093	96	0.851	0.579	0.272
0.20	–	–	–	–	0.793	0.498	0.295
0.40	595.26	487.39	124.042	92	0.834	0.540	0.295
0.60	–	–	–	–	0.751	0.430	0.321
0.80	596.84	479.27	123.292	–	0.978	0.622	0.356
1.00	–	–	–	88	0.995	0.588	0.407

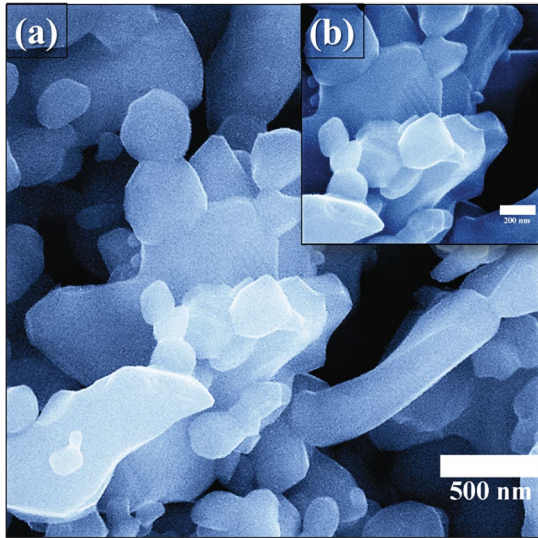


Fig. 4 FE-SEM image of $\text{Li}_{0.5}\text{Fe}_{2.5}\text{O}_4$ nanoparticles

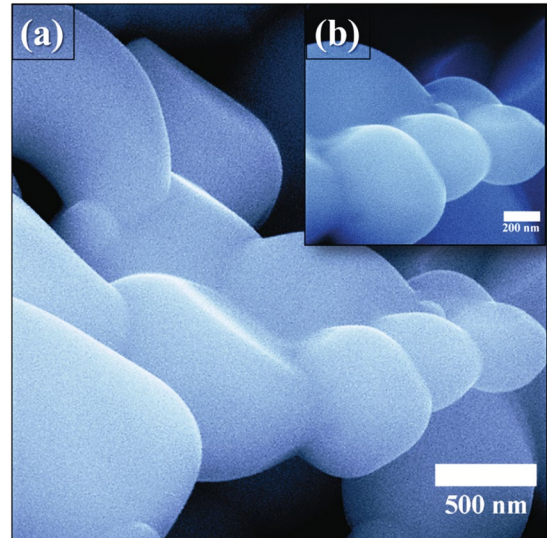


Fig. 6 FE-SEM image of LiTiFeO_4 nanoparticles

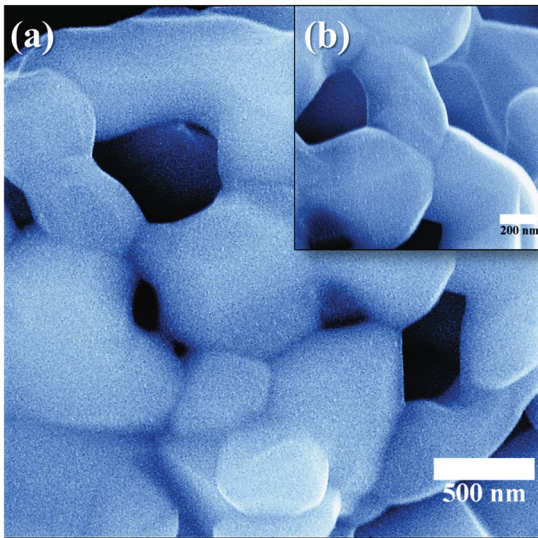


Fig. 5 FE-SEM image of $\text{Li}_{0.7}\text{Ti}_{0.4}\text{Fe}_{1.9}\text{O}_4$ nanoparticles

region was calculated by Arrhenius relation [49]. The calculated values of activation energies in the paramagnetic and ferromagnetic region are listed in Table 2. The values in

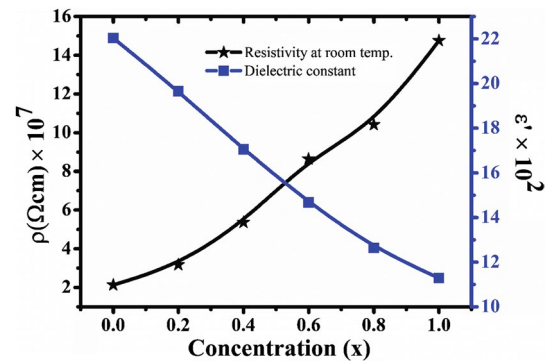


Fig. 7 Room temperature resistivity and dielectric constant at 50 Hz frequency of $\text{Li}_{0.5+0.5x}\text{Ti}_x\text{Fe}_{2.5-1.5x}\text{O}_4$ nanoparticles

the paramagnetic region are higher when compared to that of the ferromagnetic region as the conduction and valence bands splits below Curie temperature, while the bands are degenerate above the Curie temperature. Thus, it is expected that the activation energy in the paramagnetic region must be larger. The diffusion coefficient (D) was calculated using the relation [Eq. (13)] [50] and is presented in Fig. 9.

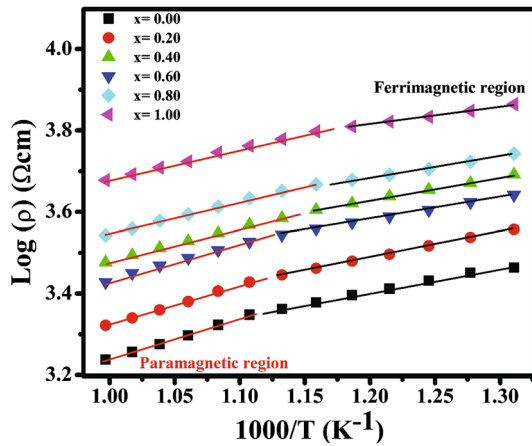


Fig. 8 Arrhenius plots for $\text{Li}_{0.5+0.5x}\text{Ti}_x\text{Fe}_{2.5-1.5x}\text{O}_4$ nanoparticles

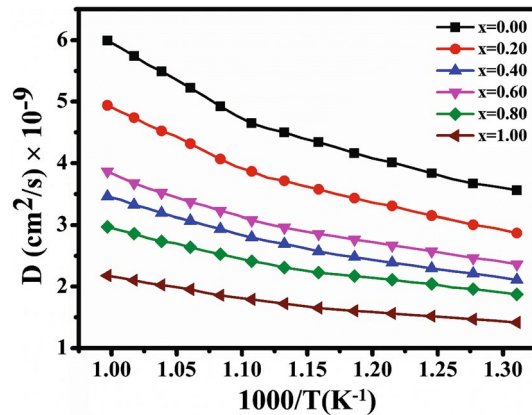


Fig. 9 Diffusion coefficient as a function of reciprocal of temperature for $\text{Li}_{0.5+0.5x}\text{Ti}_x\text{Fe}_{2.5-1.5x}\text{O}_4$ nanoparticles

$$D = \frac{\sigma k_B T}{N e^2} \tag{13}$$

where, σ is the DC electrical conductivity, k_B is Boltzmann constant and T is the temperature in Kelvin, N is the number of atoms/ m^3 , e is the electronic charge.

The Fig. 9 shows the increase in diffusion coefficient with temperature. This trend is further supported by the fact that the diffusion coefficient is inversely proportional to the DC resistivity. The room temperature DC resistivity and activation energies showed similar trend thereby indicating that the samples with high resistivity have high activation energies and vice versa.

3.5 Dielectric properties

Dielectric properties of synthesized samples were studied at room temperature by LCR-Q meter. The capacitance (C) and loss tangent ($\tan \delta$) were measured in the frequency

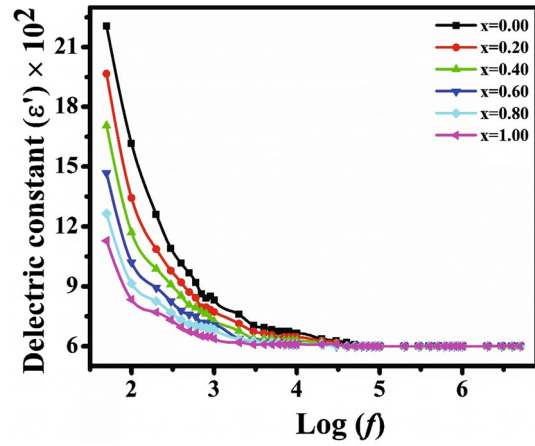


Fig. 10 Frequency dependence of dielectric constant for $\text{Li}_{0.5+0.5x}\text{Ti}_x\text{Fe}_{2.5-1.5x}\text{O}_4$ nanoparticles

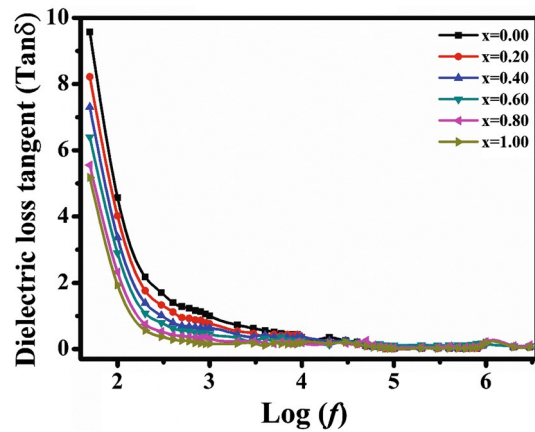


Fig. 11 Frequency dependence of dielectric loss tangent for $\text{Li}_{0.5+0.5x}\text{Ti}_x\text{Fe}_{2.5-1.5x}\text{O}_4$ nanoparticles

range 50 Hz to 5 MHz. Frequency dependence of dielectric parameters is presented in Figs. 10 and 11 respectively, also they show the changes with the composition at room temperature. The inverse relation of dielectric constant (at low frequency) with resistivity is shown in Fig. 7.

The dielectric constant (ϵ') was estimated using the Eq. (14) [12],

$$\epsilon' = \frac{Cd}{\epsilon_0 A} \tag{14}$$

where, C is the capacitance measured by LCR-Q meter, d is the thickness of the palletized sample, A is the area of the cross-section of the specimen and ϵ_0 is the permittivity of the free space. The Fig. 10 shows frequency dependence of dielectric constant. The dielectric constant is high at low frequency and rapidly decreases with increase in frequency

due to the dislocations, voids and defects present in the crystal structure of nano ferrites. When the frequency reaches a certain frequency limit, the electron hopping cannot follow the electric field fluctuations and tends to decrease the dielectric constant with increasing frequency. The decreasing behavior of dielectric constant with increasing frequency is owing to the fact that at higher frequencies, any effect contributing to polarization is found to show lagging behind the applied field. At high frequencies, the dielectric constant has less value due to low resistivity and becomes less dependent on frequency. The variation of dielectric constant with frequency can be attributed to the space charge polarization due to an inhomogeneous dielectric structure as discussed by Maxwell and Wagner [51] and Koops' theory. As Ti^{4+} and Li^+ content increase in Li-ferrite, the values of dielectric constant decrease. At low frequencies, the difference in dielectric constant is more as compared to high frequencies. With decreasing Fe ions which are responsible for polarization and the decreasing trend of grain size with concentration as discussed in FE-SEM results; the decrease in dielectric constant for the present system is expected. Similar results are available in the literature for spinel ferrites [52].

Frequency dependence of dielectric loss tangent is illustrated in Fig. 11. The Fig. 11 shows an exponential decrease of dielectric loss tangent with an increase in frequency, following the same trend observed in dielectric loss. The decrease of loss tangent with increasing frequency is due to the fact that the hopping frequency of charge carriers cannot follow the changes of the externally applied electric field beyond a certain frequency limit. The obtained results are in good agreement with the literature reports available for Li-ferrite [53].

4 Conclusion

The substitution of Ti^{4+} ions in Li-ferrite has been successfully achieved by using sol-gel auto combustion technique. XRD analysis revealed the single phase cubic spinel structure of the synthesized samples wherein ordered α -phase is observed in pure Li-ferrite and disordered β -phase is observed in Ti^{4+} ion substituted samples. The lattice parameter was found to be comparable with the JCPDS data for Li-ferrite. IR spectra show absorption bands at ~ 600 and $\sim 480 \text{ cm}^{-1}$ confirming the formation of spinel ferrite skeleton. FE-SEM images showed grains of ~ 88 – 96 nm with spherical morphology. The substitution of Ti^{4+} ions greatly influenced the electrical and dielectric properties of Li-ferrites. DC resistivity increased with Ti^{4+} ion substitution, the room temperature dielectric properties of the system as a function of frequency showed the normal dispersion behavior and the values were found to be lower as compared to that for Li-ferrite after Ti^{4+} ions substitution.

References

1. A. Goldman, *Modern Ferrite Technology* (Springer, New York, 2006)
2. A.P. Surzhikov, A.V. Malyshev, E.N. Lysenko, V.A. Vlasov, A.N. Sokolovskiy, *Ceram. Int.* (2017)
3. S. Soreto, M.G.M. Valente, L. Costa, *Magn. Spinel-Synth. Prop. Appl. InTech* (2017)
4. Z.A. Gilani, M.F. Warsi, M.N. Anjum et al., *J. Alloys Compd.* **639**, 268–273 (2015)
5. G.G. Rao, K. Samatha, S. Bharadwaj, M.P. Dasari, *Mod. Phys. Lett. B* **30**, 1650311 (2016)
6. N.K. Saxena, N. Kumar, P.K.S. Pourush, S.K. Khah, *OAM-RC* **4**, 328–331 (2010)
7. P.B. Braun, *Nature* **170**, 1123–1123 (1952)
8. T. Kutty, M. Nayak, *J. Alloys Compd.* **269**, 75–87 (1998)
9. E. Wolska, P. Piszora, K. Stempin, C.R.A. Catlow, *J. Alloys Compd.* **286**, 203–207 (1999)
10. S. Gyergyek, D. Makovec, A. Kodre, I. Arcon, M. Jagodic, M. Drogenik, *J. Nanopart. Res.* **12**, 1263–1273 (2010)
11. S. Franger, F. Le Cras, C. Bourbon, H. Rouault, *J. Power Sourc.* **119**, 252–257 (2003)
12. M. Srivastava, A.K. Ojha, S. Chaubey, P.K. Sharma, A.C. Pandey, *Mater. Sci. Eng. B* **175**, 14–21 (2010)
13. V.R. Bhagwat, M.N. Sarnaik, V.D. Murumkar, K.M. Jadhav, *IAR-JSET* **4**, 36–38 (2017)
14. S.S. Bhatu, V.K. Lakhani, A.R. Tanna et al., *IJPAP* **45**, 596–608 (2007)
15. G.H. Kale, A.V. Humbe, S.D. Birajdar, A.B. Shinde, K.M. Jadhav, *J. Mater. Sci.* **27**, 2151–2158 (2016)
16. A.V. Humbe, A.C. Nawle, A.B. Shinde, K.M. Jadhav, *J. Alloys Compd.* **691**, 343–354 (2017)
17. L. Ai, J. Jiang, *Curr. Appl. Phys.* **10**, 284–288 (2010)
18. S.E. Shirsath, R.H. Kadam, A.S. Gaikwad, A. Ghasemi, A. Morisako, *J. Magn. Magn. Mater.* **323**, 3104–3108 (2011)
19. J. Azadmanjiri, S.S. Ebrahimi, H. Salehani, *Ceram. Int.* **33**, 1623–1625 (2007)
20. M.K. Abbas, M.A. Khan, M. Faiza et al., *Ceram. Int.* **43**, 5524–5533 (2017)
21. T.A. Atia, P. Altimari, E. Moscardini, I. Pettiti, L. Toro, F. Pagnanelli, *Chem. Eng. Trans.* **47**, 151–156 (2016)
22. A.M. A-Dief, S.M. A-Fatah, *BJBAS*, (2017)
23. M.A.L. Klein, A. Jitianu (ed) *Handbook of Sol-gel Science and Technology* (Springer, Dordrecht, 2017)
24. S.S. Deshmukh, A.V. Humbe, A. Kumar, R.G. Dorik, K.M. Jadhav, *J. Alloys Compd.* **704**, 227–236 (2017)
25. A. Maria, A. Alberto, T.I. Maria et al., *Fuel* **195**, 38–48 (2017)
26. V.J. Deshmukh, P.S. Jadhav, K.K. Patankar, S.S. Suryawanshi, V.R. Puri, *NJGC* **02**, 122–127 (2012)
27. V. Verma, V. Pandey, V.N. Shukla, S. Annapoorni, R.K. Kotnala, *Solid State Commun.* **149**, 1726–1730 (2009)
28. J. Bhattacharya, C. Wolverton, *J. Electrochem. Soc.* **161**, A1440–A1446 (2014)
29. A.G. Flores, L. Torres, M. Zazo, V. Raposo, J. Iñiguez, *Appl. Phys. Lett.* **67**, 427–429 (1995)
30. J.S. Kounsalye, A.V. Humbe, P.P. Khirade, A.R. Chavan, K. Jadhav *AIP Conference Proceedings* AIP Publishing, (2017)
31. S. El Shabrawy, C. Bocker, D. Tzankov, M. Georgieva, R. Harizanova, C. Rüssel, *J. Appl. Phys.* **121**, 133903 (2017)
32. S. Dey, A. Roy, D. Das, J. Ghose, *J. Magn. Magn. Mater.* **270**, 224–229 (2004)
33. M. Schieber, *J. Inorg. Nucl. Chem.* **26**, 1363–1367 (1964)
34. A. Navrotsky, H.S.C. O'Neill, *Am. Miner.* **68**, 181–194 (1983)
35. P. Coppens, *X-ray Charge Densities and Chemical Bonding* (IUCr, New York, 1997)

36. M. Irfan, U. Khan, W. Li, W. Kong, K. Javed, X. Han, J. Alloys Compd. **691**, 1–7 (2017)
37. S.S. More, R.H. Kadam, A.B. Kadam, D.R. Mane, G.K. Bichile, Open Chem. **8**, 419–425 (2010)
38. A.T. Raghavender, K.M. Jadhav. Int. J. Mod. Phys. B **23**, 223–234 (2009)
39. H.Y. Hwang, S.W. Cheong, P.G. Radaelli, M. Marezio, B. Batlogg, Phys. Rev. Lett. **75**, 914 (1995)
40. R.D. Shannon, Acta Crystallogr. Sect. A **32**, 751–767 (1976)
41. V. Vinayak, P.P. Khirade, S.D. Birajdar, D.B. Sable, K.M. Jadhav, JOSOC **29**, 1025–1032 (2016)
42. R.D. Waldron, Phys. Rev. **99**, 1727–1735 (1955)
43. S. Hafner, Z. Kristallogr, Cryst. Mater. **115**, 331–358 (1961)
44. S.A. Mazen, F. Metawe, S.F. Mansour, J. Phys. D **30**, 1799 (1997)
45. C.M. Hurd, Contemp. Phys. **23**, 469–493 (1982)
46. S.R. Nimbore, D.R. Shengule, S.J. Shukla, G.K. Bichile, K.M. Jadhav, J. Mater. Sci. **41**, 6460–6464 (2006)
47. V.S. Sawant, A.A. Bagade, K.Y. Rajpure, Phys. B **474**, 47–52 (2015)
48. S. Yashonath, P. Santikary, J. Phys. Chem. **97**, 3849–3857 (1993)
49. S.E. Shirsath, M.L. Mane, Y. Yasukawa, X. Liu, A. Morisako, Phys. Chem. Chem. Phys. **16**, 2347–2357 (2014)
50. A. Hirao, H. Nishizawa, M. Sugiuchi, Phys. Rev. Lett. **75**, 1787 (1995)
51. F. Kremer, A. Schönhal, *Broadband Dielectric Spectroscopy* (Springer, Berlin, 2012)
52. P.P. Hankare, R.P. Patil, U.B. Sankpal et al., J. Magn. Magn. Mater. **321**, 3270–3273 (2009)
53. M.L. Mane, V.N. Dhage, K. Ranganathan, S. M. Oak, K.M. Jadhav, Radiat Eff. Defects Solids **166**, 435–444 (2011)